AIAA Guidance, Navigation and Control Conference and Exhibit
20 - 23 August 2007, Hilton Head, South Carolina

AIAA 2007-6847

A Millimeter-Scale Lorentz-Propelled Spacecraft

Justin A. Atchison* and Mason Peck†
Cornell University, Ithaca, NY, 14853

We evaluate Lorentz force actuation as a means of propellantless propulsion for millimeter-scale spacecraft by examining the acceleration and plasma-charging benefits associated with small length scales. A fully integrated "spacecraft on a chip" is described in terms of each of the traditional spacecraft subsystems, incorporating relevant research in microfabrication. Our candidate spacecraft design periodically pulses a RF beacon for ground-based orbit determination and powers a microchip payload. The spacecraft develops a net negative charge for Lorentz orbit augmentation by using solar power to differentially charge the surfaces of a sphere and filament. Having generated a multidimensional fit of plasma-sheath data generated through NASA's Charging Analyzer Program (NASCAP), we size and optimize these two charge-carrying geometries, accounting for plasma capacitance and power requirements. In a circular orbit at 350 km, our design achieves a charge-to-mass ratio of -2.5 μC/kg resulting in a daily deviation of 18 m from a Keplerian orbit. We conclude that the Lorentz force can indeed serve as a low-mass means of infinite specific-impulse propulsion for extremely small spacecraft.

I. Introduction

System-level optimization is fundamental to successful spacecraft engineering. "Systems-on-chip" can accomplish the same tasks as a traditional system at a fraction of the mass and cost. We explore the limits of spacecraft systems engineering by proposing the design and fabrication of an entire spacecraft's functions onto a single chip. This pursuit is motivated by a variety of unique advantages. Economically, reduced satellite mass and volume correspond directly to savings in rocket fuel. Further, the manufacturing processes associated with silicon technology allow for high-volume, low-cost production. Operationally, miniaturization may enable swarms of small satellites to perform large-scale distributed sensing with high redundancy. Physically, forces typically dismissed as slow-acting perturbations can be used as a source of infinite impulse at this scale. It is this last principle that has led us to study spacecraft miniaturization as a complement to our Lorentz Augmented Orbit research, which investigates an electromagnetic means of transferring energy and momentum to a spacecraft's orbit via a rotating planetary magnetic field.

It is interesting that miniaturization could be the key to demonstrating useful propellantless propulsion, when a significant portion of current research in the field focuses on the challenges associated with the extremely large structures necessitated by the characteristically weak perturbation forces. Kilometers-long tethers and square-kilometer-sized sails have been proposed as means of collecting sufficient impulse from the space environment for useful orbital adjustment.

The intent of this work is to create the first fully self-sustaining "Spacecraft-on-Chip" (SOC) capable of demonstrating observable propulsion via the Lorentz force. Inspired by the success of the first Sputnik launch in 1957, our design is intended to be as simple as possible. For three weeks, the small sphere of Sputnik I "beeped" down to Earth its internal temperature as it orbited overhead as the first demonstration of artificial satellites. A half century later, we attempt to repeat this achievement using less than a hundred-thousandth of its mass. Our design packages the traditional spacecraft subsystems (power, attitude control, communications, etc) onto a single silicon microchip capable of traveling in a non-Keplerian orbit. This paper outlines our general design methodology, describes the nonlinear dynamics, discusses applicable technologies, and proposes a candidate design.

* Graduate Research Assistant, Sibley School of Mechanical and Aerospace Engineering, 245 Upson Hall, Student Member AIAA.
† Assistant Professor, Sibley School of Mechanical and Aerospace Engineering, 212 Upson Hall, Member AIAA.

II. Analysis

The goal of this section is to define a candidate mission. We do so with two objectives in mind: demonstrating the viability of millimeter-scale spacecraft and illustrating how the Lorentz force can provide infinite-impulse propulsion. The first objective requires that we define a spacecraft architecture that can serve a useful purpose and that survives for an appropriate lifetime. The second requires devising a propellantless space-system architecture capable of maintaining and establishing sufficient electric charge to enter an observably non-Keplerian orbit. The candidate spacecraft described here is evaluated through an analysis of mission operations, Lorentz-augmented orbital mechanics, relevant spacecraft charging mechanisms, and prospective spacecraft subsystem architectures.

A. Mission Overview

Our proof-of-concept goals suggest as simple a mission as possible. In order to validate Lorentz propulsion, we propose simultaneously launching two identical SOCs (or many pairs of identical SOCs), with one's Lorentz actuation disabled. Because the two spacecraft would be identical in every respect, differential drag and related effects would be minimized. Then, deviation of one's orbit from the other would be due primarily to the Lorentz force. If the two systems are identical, this demonstration is single-fault tolerant at a high level. A four-phase operational sequence of events supports these measurements:

1. Launch / Separation

A circular LEO injection serves as the baseline launch. A likely deployment device would eject the SOCs from a parent spacecraft using adhesive that degrades in UV, a release of localized compressive load on the chip due to thermal expansion in sunlight, or perhaps a simple spring mechanism. Once separated from the upper stage or the primary satellite, the pair of SOC spacecraft would separate from one another in a way that minimizes unpredictable relative ΔV (e.g. the degradable UV binder approach). Lorentz-induced perturbations of the Keplerian injection orbit are measured and provide the mission-demonstration data we seek. Section B discusses the range of orbits that can that can lead to useful measurements. This versatility, coupled with a robust, extremely low-mass design, enables a wide range of secondary launch opportunities.

2. Charge / Maneuver

After separation the spacecraft establishes an electrostatic charge such that it experiences the Lorentz force as it moves with respect to Earth's magnetic field. Among the various means of producing and holding this charge that this paper considers, our preferred architecture uses solar power and differential plasma-charging effects. Such architecture offers several benefits: it maximizes the total charge-to-mass ratio, lends itself well to microscale fabrication, and requires no active means of expelling charged particles.

3. Transmit / Sense

The spacecraft communicate their position and temperature in a Sputnik-inspired fashion by periodically releasing a burst of electromagnetic energy. The frequency of these pulses is determined by the temperature of the on-board oscillator and the delay between pulses is determined by the available power. This design is one of many subsystem architectures that exploits unique benefits of the integrated circuit SOC concept. The ground segment of this project depends on appropriate ground stations to detect the beeps and infer range from data including acquisition-of-signal time, signal gain, and transmission frequency. The ranging data are assembled to reconstruct the orbit time history, demonstrating the effectiveness of the Lorentz propulsion by comparing the orbital element estimates of the uncharged SOC spacecraft to those of the charged one.

4. End of Life

Because of its propellantless architecture, an SOC spacecraft could continue to orbit and maneuver indefinitely without concern for stationkeeping propellant. Therefore, the end-of-life phase is characterized by the growth of distance between the two spacecraft to a point where the Lorentz force no longer constitutes most of the perturbation. Likely, radiation effects or thermal stress fatigue will degrade the SOC over time and will also limit the useful life.

B. Lorentz Augmented Orbit Mechanics

Our spacecraft design is driven by our proposed means of electrostatic propulsion. The spacecraft's Lorentz-augmented orbit (LAO) arises because a charged spacecraft traveling through a body's rotating magnetic field can transfer energy and momentum to and from the central body via the Lorentz force. This phenomenon is most clearly

observed in the charged dust orbiting Jupiter, where Lorentz perturbations generate unique structures in the rings. Though thorough derivations have been presented elsewhere[1,2], we briefly overview the relevant concepts here.

Let q represent the net biased electric charge and $\boldsymbol{v}_r$ the velocity relative to a magnetic field $\boldsymbol{B}$. Then, the Lorentz force $\boldsymbol{F}_L$ experienced by a charged spacecraft is

$$\boldsymbol{F}_L = q\boldsymbol{v}_r \times \boldsymbol{B}\,. \tag{1}$$

For a rotating magnetic field

$$\boldsymbol{v}_r = \dot{\boldsymbol{r}} - \boldsymbol{\omega}_B \times \boldsymbol{r}\,, \tag{2}$$

where $\dot{\boldsymbol{r}}$ is the vector time derivative of the spacecraft's position $\boldsymbol{r}$ (with magnitude r and direction $\hat{\boldsymbol{r}}$) relative to the system's barycenter in a Newtonian frame, and $\boldsymbol{\omega}_B$ is the angular velocity of the magnetic field. Based on a two-body Newtonian gravity model, the equation of motion for a charged orbiting spacecraft is

$$m\ddot{\boldsymbol{r}} = -m\frac{\mu}{r^2}\hat{\boldsymbol{r}} + q\left(\dot{\boldsymbol{r}} - \boldsymbol{\omega}_B \times \boldsymbol{r}\right)\times \boldsymbol{B}\,, \tag{3}$$

where $\mu = MG$, with parent body mass M and universal gravitational constant G. Dividing through by the spacecraft mass m, we find that Lorentz acceleration is driven by the parameter q/m, the spacecraft's charge-to-mass ratio. The magnetic field at Earth is approximated by its dominant mode, a dipole with magnetic induction B_0 measured at a reference distance r_0 is

$$\boldsymbol{B} = -B_0\left(\frac{r_0}{r}\right)^3\left(2\cos\delta\,\hat{\boldsymbol{r}} + \sin\delta\,\hat{\boldsymbol{\delta}}\right), \tag{4}$$

expressed in right-handed spherical coordinates defined by radial $\hat{\boldsymbol{r}}$, azimuthal $\hat{\boldsymbol{\theta}}$, and polar $\hat{\boldsymbol{\delta}}$ directions. We simplify the field by aligning its spin with its parent body (neglecting the dipole tilt). Previous work has demonstrated that this simplification captures the governing physics with little loss of accuracy[2].

Though LAO has many potential applications, we focus our work on its simplest demonstration: non-Keplerian LAO effects in a circular orbit at the magnetic field's equator. Figure 1 indicates the directions of the Lorentz force vectors for a charged body in a prograde orbit subject to these conditions. Here, the directions of the central body's spin axis and magnetic field vector are defined by the right-hand rule. Earth's geographic north pole corresponds to its magnetic south pole; hence the magnetic field's direction is shown as roughly opposite to its spin direction. The spacecraft's inertial and relative velocities lie perpendicular to its position vector and the magnetic field vector, constraining the Lorentz force's line of action along the radial direction $\hat{\boldsymbol{r}}$. These constraints imply that the Lorentz force cannot do work on the orbit ($\boldsymbol{F}_L \cdot \dot{\boldsymbol{r}} = 0$) or alter its angular momentum ($\boldsymbol{r} \times \boldsymbol{F}_L = 0$). Therefore, the Lorentz force can alter only the spacecraft's potential energy, effectively changing the magnitude of gravity. The ratio of the magnitudes of Lorentz and gravitational accelerations is given by the dimensionless parameter β:

$$\beta = \frac{q}{m}\frac{B_0}{\mu}\frac{r_0^{\,3}}{r}\left[\sqrt{\frac{\mu}{r}} \pm \omega_B r\right], \tag{5}$$

where the plus sign denotes a retrograde circular orbit, and the minus sign denotes a prograde circular orbit. For the sake of compatibility with secondary-launch opportunities, we focus on prograde orbits. Figure 2 plots the prograde acceleration ratio β for a charged spacecraft orbiting Earth as a function of radial distance for a unit positive charge-to-mass ratio (1 C/kg). As illustrated in the figure, the Lorentz force approaches zero as the spacecraft approaches geostationary orbit, where the spacecraft's relative velocity approaches zero $\dot{\boldsymbol{r}} = \boldsymbol{\omega}_B \times \boldsymbol{r}$. In view of β's steep reduction with increasing altitude, we concentrate on LEO to maximize the perturbation.

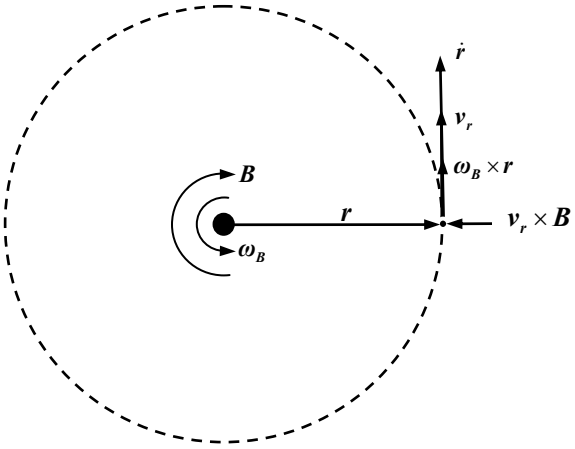

Figure 1. Vector depiction of the Lorentz force at various locations in a prograde, circular, magnetic-equatorial orbit.

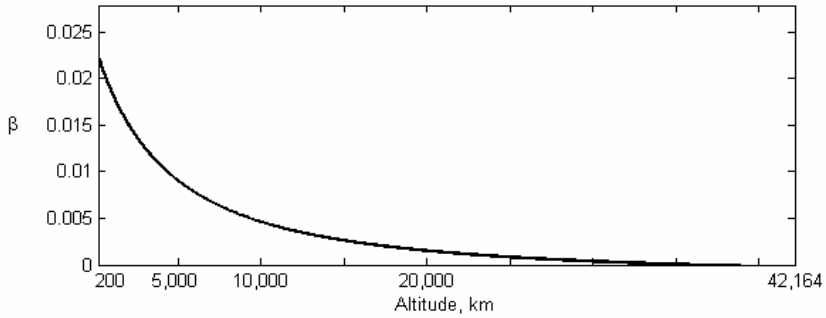

Figure 2. Magnitude of acceleration due to Lorentz force relative to gravitational acceleration for a charged body with a unit charge-to-mass ratio (1 C/kg) in a circular orbit from LEO to geostationary orbit.

From force balance in the radial direction, similar to Kepler's third law but augmented with the Lorentz effect, the following result relates the magnitude of a charged spacecraft's angular velocity ω to its orbital radius[1]:

$$\frac{q}{m}(\omega - \omega_B)B_0 {r_0}^3 + \omega^2 r^3 = \mu \,. \tag{6}$$

In terms of radius as the dependent variable, the equation becomes

$$r = \sqrt[3]{\frac{1}{\omega^2}\left(\mu - \frac{q}{m}(\omega - \omega_B)B_0 {r_0}^3\right)} \,. \tag{7}$$

Alternatively, the angular velocity expressed in terms of radius yields two solutions

$$\omega = \frac{-\frac{q}{m}B_0 {r_0}^3 \pm \sqrt{\left(\frac{q}{m}B_0 {r_0}^3\right)^2 + 4r^3\left(\mu + \frac{q}{m}\omega_B B_0 {r_0}^3\right)}}{2r^3}, \tag{8}$$

where addition is associated with a prograde orbit and subtraction with a retrograde orbit.

These results represent two LAO maneuvers that can be easily accomplished with a charged spacecraft. Figure 3a shows a circular formation that is impossible with purely Keplerian orbits: charged spacecraft with the same angular velocity as uncharged spacecraft at separate altitudes. Alternatively, Figure 3b illustrates a charged spacecraft in a circular orbit of the same radius as an uncharged spacecraft, but with a different angular velocity. For the second case, the along-track separation $\Delta\theta$ per day between the two spacecraft is evaluated with Earth conditions at an altitude of 350 km and plotted in Figure 4 on a log scale. For a prograde orbit, a positive charge-to-mass ratio causes the spacecraft to lag behind an uncharged spacecraft, and a negative charge-to-mass ratio leads an uncharged spacecraft. This figure suggests types of LAO-driven deviations from a Keplerian orbit that may be observable, even for relatively low charge-to-mass ratios. To avoid the subtle sequence of DV maneuvers necessary to create the formation in Figure 3a, our candidate mission is therefore to release a charged spacecraft-on-a-chip at about 350 km altitude and to measure its daily deviation from an uncharged orbit.

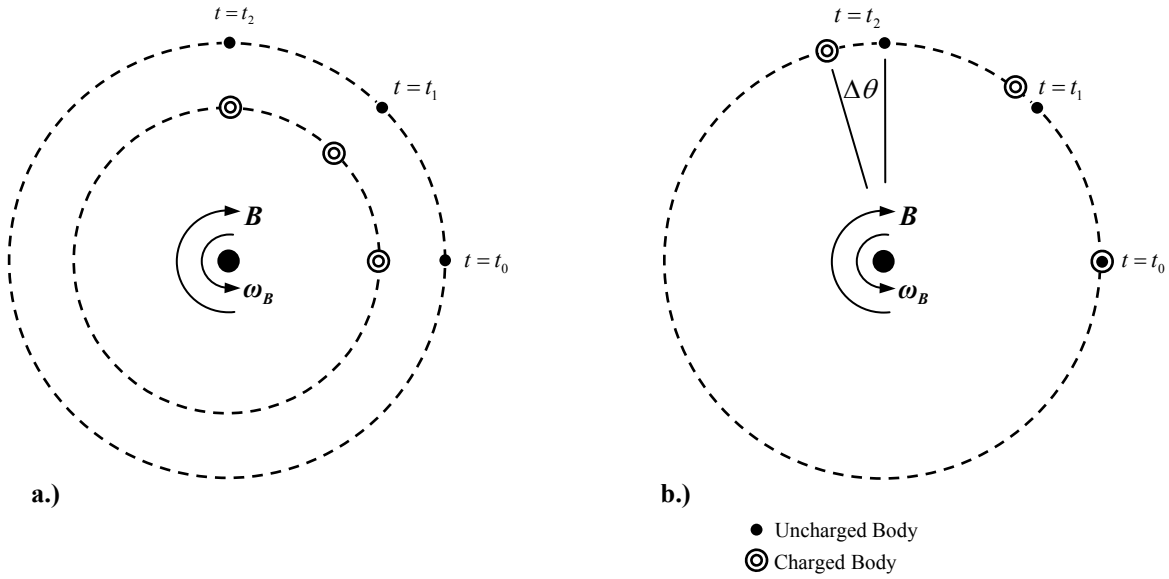

Figure 3. Deviations from non-Keplerian orbits by charged spacecraft in circular magnetic-equatorial orbits. a.) constant-radius formation flying and b.) along-track separation

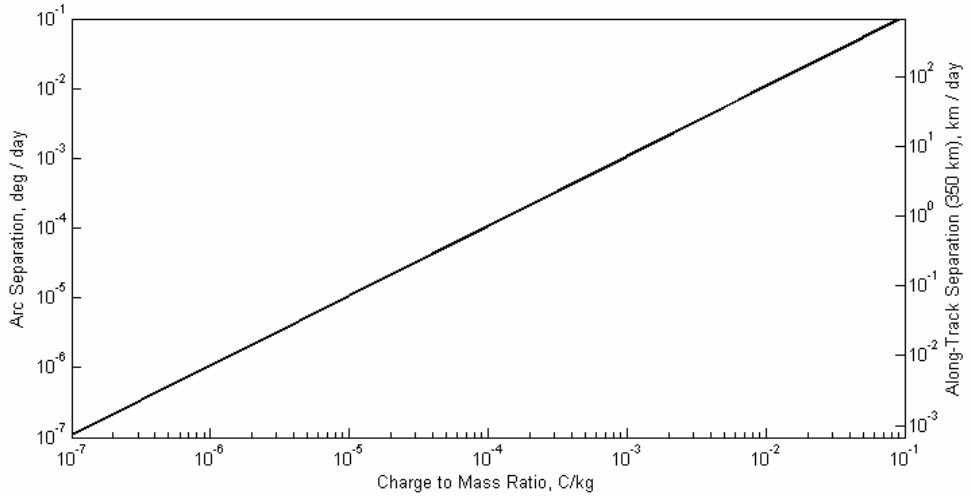

Figure 4. Arc separation between a charged and uncharged spacecraft in a prograde circular orbit at 350 km altitude.

C.Space Plasma Effects

Charge allows the spacecraft to interact with a planet's magnetic field and transfer energy from the planet's rotation into the spacecraft's orbit. In a perfect vacuum, orbital adjustment via the Lorentz Force is essentially power-free because the charge remains on the spacecraft indefinitely. However, charging interactions with the LEO plasma environment leads to some leakage of charge. This leakage rate, or plasma current, dictates the power requirement. However, maintaining this spacecraft charge is the only aspect of an LAO that demands power. Indeed, coupling between the Earth's magnetic field and plasma necessitate an optimization between the effectiveness of LAO and the power demands associated with the local plasma density. Though it is unreasonable to adequately discuss the physics of spacecraft plasma charging, we attempt to offer a cursory overview of the most relevant mechanisms.

A conductive body orbiting in a plasma attains a non-zero equilibrium potential φ_s, determined by the incident currents associated with processes such as local plasma attraction, photoelectric emissions, and artificial (e.g. electron-beam) currents. Accounting for a body's self-capacitance C (roughly, its ability to hold charge on its surface), this equilibrium potential corresponds to an equilibrium charge:

$$q = C\phi_s \,. \tag{9}$$

For a desired charge to be established, a biased potential must be generated on a body with sufficiently large self-capacitance. To maintain this potential, current must be provided to negate the natural charging mechanisms, motivating our research into spacecraft charging models. As for self-capacitance, our design focuses on the most well-understood charging geometries: a sphere and a thin wire.

The LEO environment is treated as a plasma consisting of an equal number-density of electrons and positive ions (i.e. a quasi-neutral plasma). An initially neutral body in a static quasi-neutral plasma will maintain a near-zero floating potential. However, LEO spacecraft traverse the local plasma with mesosonic velocities. That is to say, their velocity is much greater than the thermal velocity of the massive positive ions (primarily O^+ within our region of interest), but much less than the thermal velocity of electrons. For this reason the spacecraft interacts with the two polarities of particles differently.

Electron velocities exceed that of the spacecraft, meaning that electrons can all but instantaneously collect or evacuate a region around the spacecraft. As they approach a positively biased body, their charge cancels a portion of the electric field, reducing the net attraction experienced by other electrons. The result is a steady-state electron distribution around the charged body known as a plasma sheath. A sample plasma potential profile associated with a sheath is illustrated in Figure 5. The potential of the plasma decreases with distance from the body until it reaches the quasi-neutral plasma potential at its outer sheath edge, the point at which the electric field associated with the body is cancelled (or shielded) by the distribution of oppositely charged particles around it.

The current associated with these electrons is defined as the electron thermal current

$$I_{th} = nq_e A_{SO}\sqrt{\frac{T}{2\pi m_e}} \tag{10}$$

where n is the unperturbed electron number density, q_e is the charge of an electron, A_{SO} is the surface area defined by the outer sheath edge, T is the quasi-neutral temperature of the plasma reported in eV, and m_e is the mass of an electron. Though not explicitly shown, thermal current has a strong dependence on the body's potential through the sheath surface area which will be discussed below.

With respect to positive ions, LEO spacecraft velocities are supersonic. Positive ions within the outer sheath edge are attracted to the negatively charged body, but are unable to react quickly enough to collect around the body. Only the ions that are directly impacted by the area enclosed by the outer sheath edge can react with the spacecraft. Of these, a portion η_{ram} contact the spacecraft and impart their charge. This mechanism is known as ram current

$$I_{ram} = \eta_{ram} nq_i v_r A_{ram} \,, \tag{11}$$

where n is the unperturbed ion number density, and q_i is the charge of the ion species. A_{ram} is related to the frontal area (normal to $\boldsymbol{v_r}$) of the spacecraft's outer sheath edge[3]. A ram efficiency of 0.7 has been suggested as an estimate[9], which we adopt here. The inability of positive ions to collect around a negatively charged spacecraft generates a region with an absence of elections. That is to say, electrons are repelled from the spacecraft, while

positive ion densities remain essentially unaffected. The result is a positive charge distribution surrounding the spacecraft comparable to Figure 5.

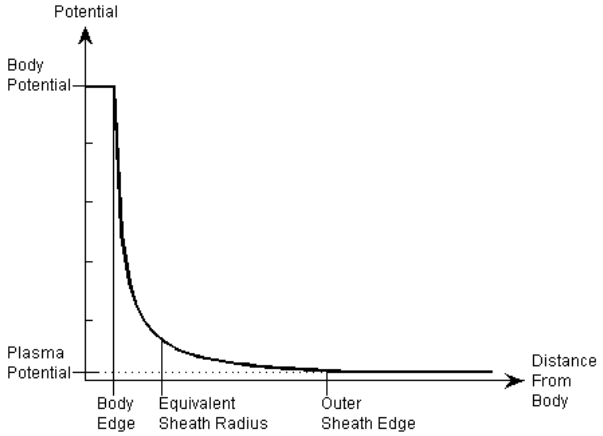

Figure 5. Illustration of plasma potential as a function of distance from the surface of a spacecraft.

1. Sphere Charging

For a sphere, the potential distribution outside the body (as depicted in Figure 5) is

$$\phi(x) = \phi_s \frac{x}{r_s} \exp\left(\frac{-(x - r_s)}{\lambda_D}\right), \tag{12}$$

where φ_s is the potential of the sphere, r_s is the radius of the sphere, and x is the distance from the surface of the sphere[4]. The coefficient in the exponent is a characteristic dimension of the plasma, the Debye length

$$\lambda_D = \sqrt{\frac{\varepsilon_0 T}{n q_e^{\,2}}}\ , \tag{13}$$

where ε_0 is the permittivity of free space. For low sphere potentials, the effective ram area is defined by a circle with a radius of a few Debye lengths. However, as the body's potential increases, the outer sheath edge increases as well. A survey of space plasma literature resulted in two models used to estimate the outer sheath edge for a charged sphere.

The first model used to predict this increased outer sheath size S_O for a sphere with a high potential in a plasma environment is the Child-Langmuir Law

$$S_O = \frac{\sqrt{2}}{3} \lambda_D \left(\frac{2\phi_s}{T}\right)^{\left(\frac{3}{4}\right)}. \tag{14}$$

The second model, by Blackwell et al, consists of an analytic fit to the numerical results of Laframboise, incorporating the sphere's radius[5,6]

$$S_O = \left(2.5 - 1.87 e^{-0.39\frac{r_s}{\lambda_D}}\right) \lambda_D \left(\frac{\phi_s}{T}\right)^{\left(\frac{2}{5}\right)}. \tag{15}$$

The differences in thermal and ram charging mechanisms suggest that power requirements are affected by the polarity of the charge on the body as well as the magnitude. A comparison of Eqs 10 and 11 indicates that the

thermal current associated with a positively charged body exceeds the ram current for an oppositely charged body for

$$v_r < \sqrt{\frac{8\pi T}{m_e}} \tag{16}$$

Indeed, LEO plasma satisfies this condition, and sample values suggest that a positively charged body requires as much as a hundred times more power than a negatively charged body.

A second pertinent sheath parameter is the equivalent sheath radius. The oppositely charged body of particles (or lack thereof, as discussed for a negatively charged body), forms a concentric shell that increases the available self-capacitance of the spacecraft. That is, the capacitance of a conductive sphere is

$$C_s = 4\pi\varepsilon_0 r_s, \tag{17}$$

while two oppositely charged concentric spheres separated by a distance S_E give

$$C_{SI} = 4\pi\varepsilon_0 r_s \frac{(r_s + S_E)}{S_E}. \tag{18}$$

This approximation treats the surrounding plasma's total charge as a single spherical shell at an equivalent distance. This distance is indicated in Figure 5 and marks the area centroid of the potential profile. A small equivalent sheath radius can significantly increase a body's self-capacitance and therefore its charge.

Noting that the two models discussed above (Eqs 14 – 15) estimate the outer sheath edge only, and are based on a relatively limited range of potentials, we turn to NASA's Charging Analyzer Program (NASCAP) for further insight.

NASCAP is an industry-standard finite-element modeling toolkit that simulates the spacecraft and plasma interactions spatially and temporally. After validating our method with a 40 kV, 1 m radius conductive sphere studied by Parker[7], we evaluated a range sphere sizes and potentials in a static LEO environment, with the constants given in Table 1. A sample of the graphical results from a NASCAP simulation for a 1 cm sphere held at 10 kV potential is shown in Figure 6.

Table 1. NASCAP Simulation Constants

Environment	LEO
Space Charge Model	Analytic, Non-Linear
Average RMS Error, V	1E-3
Plasma Density, m^{-3}	1E12
Plasma Temperature, eV	0.10
Corresponding Debye Length, m	2.351E-3
Sphere Material	Aluminum

Each simulation produces a radial plasma potential distribution around the sphere. The outer sheath edge can be found by calculating of the distance at which this potential is reduced to within the error tolerance of the solver. Next, the potential distribution around the sphere is fit to a curve of the theoretically likely form

$$\phi(x) = a_0 \frac{r_s}{x} \exp[a_1 (x - r_s)] \tag{19}$$

by solving for the unknown coefficients a_0 and a_1. This function, reminiscent of Eq 12 and Figure 5, is used to find the spatial charge density $\boldsymbol{\rho}$ via Poisson's equation

$$\nabla^2 \boldsymbol{\varphi} = \frac{-\boldsymbol{\rho}}{\varepsilon_0}. \tag{20}$$

Assuming spherical symmetry and integrating radially from the body's surface to infinity yields the net charge contained in the local plasma

$$q = -\varepsilon_0 \int_V \nabla^2 \varphi \, dV = -4\pi\varepsilon_0 a_0 r_s \left(1 - a_1 r_s\right). \tag{21}$$

This charge, equal and opposite to the charge contained on the sphere, allows us to estimate the improvement to the sphere's capacitance due to the presence of the local plasma.

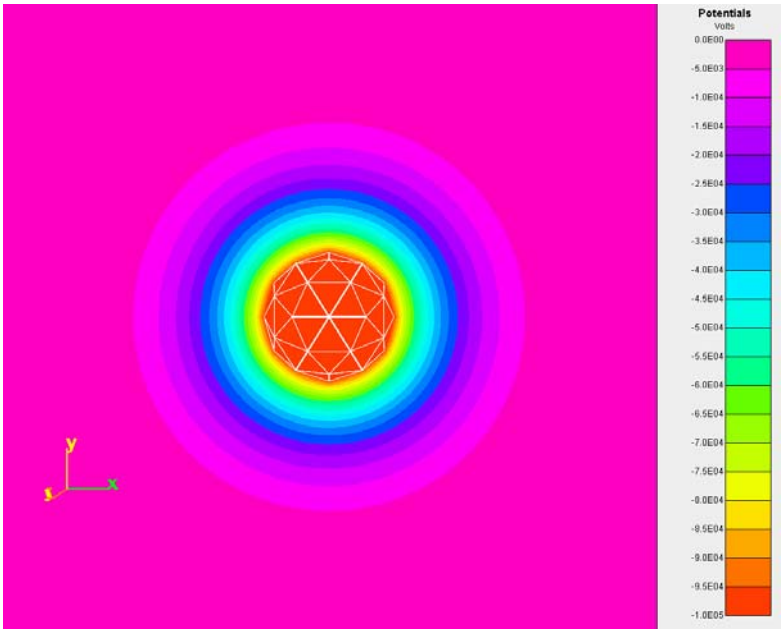

Figure 6. Sample NASCAP static plasma potential results for a sphere model charged to -10 kV potential at 350 km.

Table 2 gives the inner and outer sheath sizes calculated from these simulations. Five sphere sizes were evaluated at potential from 100V to 5.3MV, the potential of the alpha particles emitted from radioactive polonium-210 discussed at a later point in this paper. At small size scales (r_s = 0.01m and 0.1m) and high potentials (φ_s > 100kV), the equivalent sheath merges with the outer sheath as a result of the different methods of calculating these two parameters. The implication is that the equivalent sheath is no longer effective for adding useful capacitance beyond that potential. At large size scales (r_s = 10m and 100m) and low potentials (φ_s < 100V, φ_s < 1kV), NASCAP's grid format limited our ability to adequately resolve the potential profile.

Table 2. NASCAP Simulation Results, (Equivalent Sheath in meters / Outer Sheath in meters)

Potential of Sphere, kV	Radius of Sphere, m				
	0.01	0.1	1	10	100
0.1	0.04 / 0.09	0.12 / 0.22	0.31 / 0.60	-	-
1	0.10 / 0.25	0.28 / 0.60	0.79 / 1.84	1.51 / 3.46	-
10	0.45 / 0.66	0.60 / 1.88	2.12 / 4.99	3.61 / 9.74	8.06 / 18.08
100	1.86	4.85	5.87 / 13.27	13.77 / 29.56	22.00 / 60.59
500	3.24	9.82	11.10 / 24.05	32.65 / 66.20	66.83 / 186.13
5,300	9.98	23.2	32.65 / 72.67	117.76 / 133.06	228.79 / 556.88

It should be emphasized that these simulations and their corresponding results are intended to describe the plasma parameter-space in an engineering sense, not to rigorously quantify or describe the associated physics. These values were then non-dimensionalized and fit to second-order logarithmic polynomial surfaces. For a given LEO plasma

temperature T in eV and number density n in m^{-3}, the base-ten logarithm of the non-dimensionalized sphere radius and potential,

$$\lambda_r = \log_{10}\left(\frac{r_s}{\lambda_D}\right),\ \lambda_\phi = \log_{10}\left(\frac{\phi_s}{T}\right) \tag{22}$$

can be used to estimate the base-ten logarithm of the non-dimensionalized equivalent and outer sheath sizes,

$$\lambda_E = \log_{10}\left(\frac{S_E}{\lambda_D}\right),\ \lambda_O = \log_{10}\left(\frac{S_O}{\lambda_D}\right) \tag{23}$$

according to the second order polynomial surface-fit

$$\lambda_{E,O} = c_1\lambda_r{}^2 + c_2\lambda_r\lambda_\phi + c_3\lambda_r + c_4\lambda_\phi{}^2 + c_5\lambda_\phi + c_6 \tag{24}$$

with coefficients given in Table 3 below.

Table 3. Coefficients for Surface Fits Given by Equation 22

	Equivalent Sheath	Outer Sheath
c_1	-0.007934	-0.014351
c_2	-0.010351	0.017511
c_3	0.425960	0.367490
c_4	0.009198	-0.003839
c_5	0.419800	0.446000
c_6	-0.311750	0.020039

2. Filament Charging

For a filament, the charging mechanisms are closely related. As in the case of a sphere, a charged filament attracts or repels electrons such that a sheath develops. The outer edge of this sheath represents the distance at which the electric field of the filament is negated by the surrounding plasma's distribution. The equivalent sheath acts as a concentric cylindrical shell of opposite charge, increasing the geometry's capacitance according to

$$C_f = \frac{2\pi\varepsilon_0 L_f}{\ln\left(\frac{r_f + S_I}{r_f}\right)} \tag{25}$$

where L_f is the length of a filament with radius r_f. Choinière gives models for estimating the equivalent sheath radius based on numerical and experimental work[8]:

$$2.554\left(\frac{S_I}{\lambda_D}\right)^{1.325}\ln\left(\frac{S_I}{r_f}\right) = -\frac{\phi_s}{T}, \tag{26}$$

$$S_I = 0.123\,\lambda_D\left(\frac{|q|}{L_f}\frac{1}{\varepsilon_0 T}\right)^{0.755}. \tag{27}$$

This model is valid for potentials and filament radii that satisfy the two conditions:

$$r_f < 0.1\lambda_D$$

$$\phi_s > \frac{200}{2\pi}\ln\left(\frac{S_I}{r_f}\right).$$

Power collection for a filament differs from that of a sphere. Charged bodies with characteristic lengths (the radius for spheres and cylinders) smaller than the local Debye length, orbit-motion-limited (OML) current collection dictates the power requirements:

$$I_{OML} = \frac{nq_e A_f}{\pi}\sqrt{\frac{2q_e|\phi_s|}{m_{i,e}}}, \tag{28}$$

where A_f is the total surface area of the filament and $m_{i,e}$ is the mass of the ions or electrons attracted by the filament's charge. For positively charged filaments, OML dictates the most efficient electron collection current. Alternatively, OML's mass dependence implies that a negatively charged filament in LEO will collect fewer massive ions than ram charging would predict.

Figure 7 gives a plot of the linear charge density and sheath size subject to these bounds for a 10 μm radius filament, though it should be noted that the sheath is only very weakly dependent on the filament radius (as dictated by the bounds). The filament radius dictates a minimum potential of 300 V to satisfy the conditions of applicability.

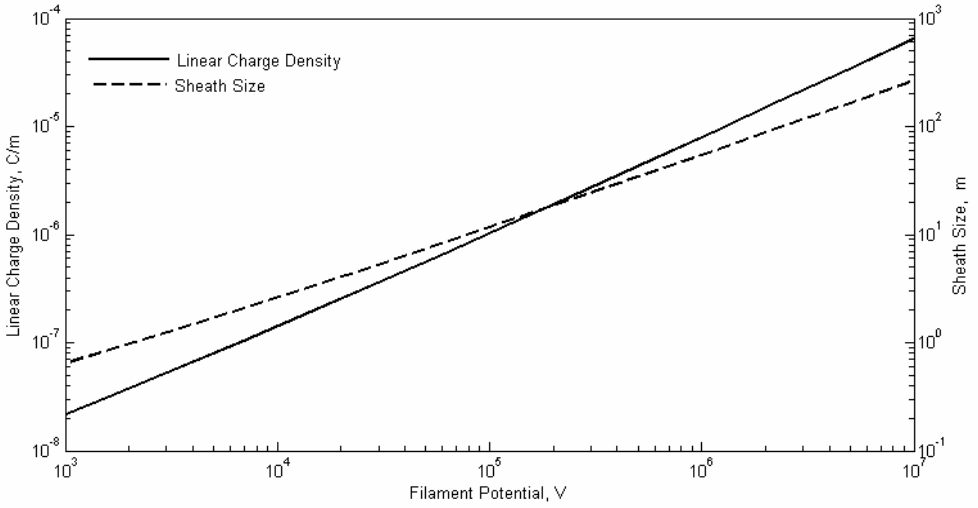

Figure 7. Linear charge density and sheath size as functions of negative potential potential for a 10 μm radius filament.

3. Differential Charging

Geometry and polarity can result in different plasma-charging mechanisms. We exploit this difference to enable a net spacecraft charge using a potential source as proposed by Hoyt and Minor[9]. This method offers useful and controllable charge, as well as the advantage of requiring only a sufficient potential source.

In a vacuum, if two conductive spheres are connected to the terminals of a perfect battery, each sphere reaches a potential equal to half of the battery's potential and with opposing polarities. However, in a plasma environment, the spheres' opposite polarities generate dissimilar currents, resulting in dissimilar sphere potentials[3]. At LEO where thermal charging exceeds ram charging, the positive sphere's (henceforth referred to as the cathode) equilibrium potential can decrease almost to zero. The perfect battery continues to maintain the potential difference between the two spheres, requiring that the negative sphere's (anode) equilibrium potential consequently increase. The system then may then act as a single body with a net negative charge.

This system is somewhat inefficient, in that a portion of the net charge is reduced by the cathode's nonzero equilibrium potential. However, we can improve efficiency by varying the cathode's geometry. The goal is for the capacitance of the anode to far exceed the cathode so that at the equilibrium potential, the net charge on the system is decidedly negative. For example, one end can be a large sphere and the other a thin filament. Since OML is the most efficient current collection method, this latter example represents a mass-efficient charging architecture.

4. Alternative Charging Concepts

The advantages and capabilities of the differential-charge architecture discussed above makes it a clear candidate for our millimeter-scale spacecraft. However, this solution came about after exploring a number of possible charging mechanisms. For completeness, we briefly outline them here.

a. Passive Charging

Once inserted into an orbit, the chip experiences currents due to ram charging, thermal attraction, photoemission, and secondary interactions. Differences in these mechanisms cause a spacecraft to generally achieve a non-zero potential. For a sufficiently high ratio of capacitance to mass, these potential variations could prospectively perturb an orbit in a measurable manner, demonstrating LAO. Such is the case for dust in Jupiter's orbit, after all. A body in LEO typically attains an equilibrium potential of a few volts positive[4], though the plasma environment and thus charging conditions vary significantly both temporally and spatially. It is conceivable that a spacecraft could achieve novel resonances (again, as observed in dust at Jupiter). However, passive charging seems less desirable than other options because LEO equilibrium potentials are generally too low. Furthermore, the uncontrollable and unpredictable nature of this potential severely limits applications.

b. Photoemission Charging

One of the natural currents a spacecraft experiences is photoemission charging. Current is generated when a photon impacts a spacecraft's surface and liberates an electron. A continuous ejection of electrons represents a current that depends on the energy of the impacting photon (i.e. its frequency), the specific material properties (photoemission yield, surface treatment), and the angle of incidence. Currents associated with photoemission are on the order of 10^{-9} A/cm^2 (Ref. 4). In an effort to maximize this current, a thin film of high-yield material could be deposited onto the surface of the charge geometry. Similar to passive charging, one can conceive of resonances incorporating the periodic solar eclipse or even forced by applying materials of different yields to different sides of the spacecraft.

Kasha calculates the floating potential to be 0.6 V for an aluminum 1 m radius sphere in a circular orbit at 350 km experiencing photoemission charging (Ref. 10). Based on this value, it seems unlikely that photoemission current can establish charge-to-mass ratios sufficient to demonstrate observable orbit modification, let alone serve as a useful means of propulsion.

c. Radioactive Emission

Another charging concept attempts to use radioactive emission as a current source. As radioisotopes naturally decay, they emit energetic particles. In the case of alpha decay, these particles are helium nuclei with a +2 charge. For beta decay, electrons or positrons are emitted with charge -1 or +1 respectively. These emissions represent a current which would alter the floating potential of a body[4]. Research on SPEAR suggests that the potential can reach the emitted particle's energy given sufficient current. This implies that a spacecraft could achieve a potential on the order of megavolts if the current is sufficient to overcome that of the incident plasma.

This method is not quite propellantless, in that it requires the launch of an initial mass of radioisotope that depletes itself over time. Only the particles that are ejected in a direction away from spacecraft contribute to the body's potential; the others remain within the isotope and dissipate their emission energy as heat. This principle suggests that current efficiency can be maximized if the isotope is deposited in a thin film onto the outer surface of the body. This current might also be modulated by altering the surface geometry or exposure. Note that this calculation uses the emission of particles to impart a charge, not momentum.

The following brief analysis of radioactive emissions as a means of thrust shows that significant orbital perturbations are not feasible. A sample of radioactive material decays exponentially according to:

$$N(t) = N_0 \exp\left(\frac{-t}{\tau}\right) \tag{29}$$

where N is the number of atoms in the sample with initial value N_o at time $t = 0$, and τ is the isotope's mean life given in units of time. The decay current is determined by the product of the decay rate, the charge of the emitted particles q_{iso}, and an efficiency term η_{iso} that accounts for particles unable to escape the spacecraft. Using the isotope's density ρ_{iso} (with units atoms/kg), we find an expression for decay current

$$I_{iso} = \eta_{iso} q_{iso} \cdot \frac{dN(t)}{dt} = -\eta_{iso} \frac{q_{iso}\, \rho_{iso}\, m_{0iso}}{\tau} \exp\left(\frac{-t}{\tau}\right). \tag{30}$$

Equating this current to the incident ram current allows us to solve for the spacecraft's floating potential over time. The results of these calculations for Polonium-210, a highly energetic alpha emitter (5.3 MeV), applied to a centimeter radius sphere, after one year's decay, are shown in Figure 8. It is clear from these figures that the polonium is incapable of supplying enough current to attain charge-to-mass ratios sufficient for useful LAO maneuvers. The current associated additional radioactive material is not large enough to augment the total charge-to-mass ratio.

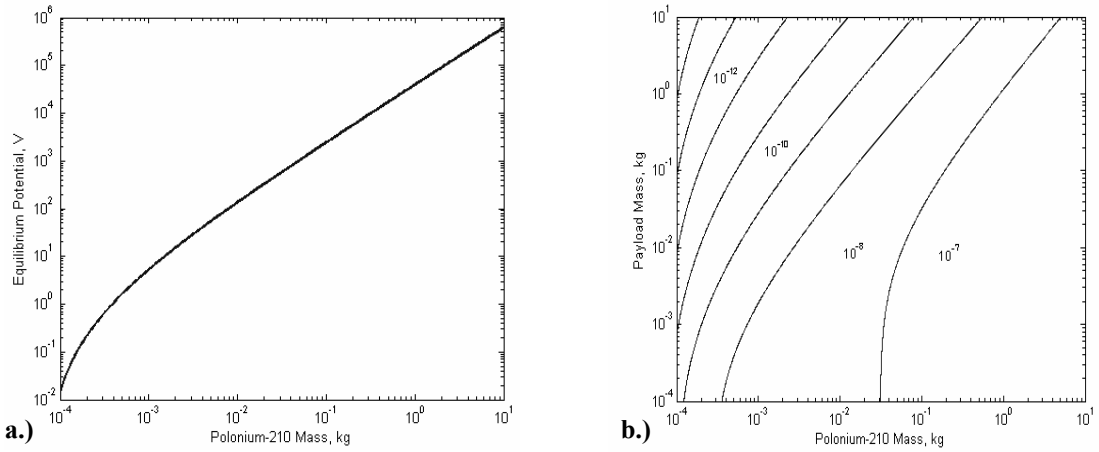

Figure 8. a.) Equilibrium potential in V as a function of polonium-210 mass and b.) Charge-to-mass ratio in C/kg as a function of polonium-210 mass and payload mass for a 1 cm radius sphere after 1 yr at 350 km.

d. Pyroelectric Emission

Yet another means of emitting charge from a body is the use of pyroelectric crystals. When subjected to changes in temperature, pyroelectric crystals rapidly polarize, generating intense electric fields. These fields can accelerate ions or electrons in a uniform beam, with electron energies on the order of 100 keV. If the temperature reverses, the electric field also reverses, attracting the opposite charge[11].

Differences in particle mobility could be instrumental in establishing a biased charge for rapid thermal cycles. That is, the current of ions attracted to the negative induced field is less than the electron current when the field reverses. An alternating current applied to a thermocouple could potentially generate extremely high potentials. Passively, the small thermal mass and large temperature gradients associated with solar eclipses could feasibly enable unique resonant orbits. Having observed these peculiar crystals firsthand, the possibility of incorporating them into a design is attractive. However, at present this technology is too immature to be incorporated in our mass estimates with any confidence.

D. Architecture

We approach the design space with an emphasis on simplicity, feasibility, and scalability. Our goal is to accomplish something unconventional using conventional technologies. The final product is a single densely populated microchip that incorporates the eight traditional spacecraft subsystems: propulsion, power, telecommunications, attitude determination and control, structure, and thermal control.

1. Power

Solar-cell power generation is both passive and semiconductor based, making it a natural selection for power supply. We focus on silicon-based first-generation solar cells, the most well researched and fabricated photovoltaics. These cells use a single layer p-n junction diode to pass photovoltaic currents. These junctions lend themselves well to mass production silicon techniques with high volume-efficiency. By strategically connecting sets of individual cells in parallel or series, an array can be designed with specific voltage and current characteristics to accommodate LAO or payload requirements. Commercially, high efficiency cells commonly achieve specific power on the order of 200 W/kg. Presuming inefficiencies associated with integration in a MEMS environment, we conservatively model specific power as 100 W/kg. The solar array powers the charging mechanism. Thus, when the spacecraft is in eclipse, its charge will return to the local plasma potential, and the spacecraft orbit becomes temporarily Keplerian. In our final design, we calculate our solar array requirements for a spacecraft oriented at 45° from the sun vector.

2. Propulsion

With few exceptions[12], traditional propellant mechanisms such as chemical or ion thrust subsystems are unreasonable at extremely small scales, and hence propulsion discourages extreme spacecraft miniaturization. We contend that the accelerations typically classified as perturbations, namely the Lorentz force, can offer useful thrust with relatively little hardware-overhead when incorporated into our microchip architecture. Here we explore and evaluate four capacitive structures to be considered for use as the conductive geometries that maintain non-zero equilibrium potential.

a. Spherical Shell

Aside from being the most well understood geometry regarding plasma interactions, a spherical shell architecture offers noteworthy design benefits. First, it's a natural choice because it distributes charge evenly over the surface, preventing charge loss associated with sharp-point field concentrations, and making efficient use of the available surface area. Second, the sphere can act as a Faraday cage, protecting the spacecraft within from external electric fields.

Solar sail material research suggests that a likely shell candidate is CP1 polyimide film. It offers favorable mechanical properties with extremely low mass, as well as proven resistance to high thermal loads and radiation doses[13]. Sheets can be manufactured as thin as 5 μm, yielding an area density of 0.009 kg/m^2. The spacecraft could be sealed within the deflated shell at launch, and packed efficiently into a release mechanism. At the charge phase of the mission, the shell would then inflate itself to full size via electron repulsion on its surface. A transparent version, perhaps kapton coated with ITO for conductivity, can be used for solar-power collection through the sphere.

b. Filament

An extremely thin filament can efficiently store charge along its length and in the large volume of its sheath. The Lorentz force, acting along the filament, tends to pull the filament and thus the spacecraft along its direction. The Lorentz force will facilitate deployment and stabilizes its dynamics, a challenging issue associated with tethers in space. This effect can also be used to constrain the spacecraft attitude in two of the three attitude degrees of freedom.

Though the prospects of long tethers seem challenging, it should be noted that the TSS-1R electrodynamic tether mission successfully deployed a 20.7 km filament in LEO[14]. We consider commercially available 10 μm radius aluminum filaments with a linear density of 0.848 mg/m.

c. Filament Collections

This concept considers charge storage on a group of filaments bound together to form a sparse structure. One can conceive of a spherical or cylindrical capacitor built as a mesh of wires, rather than a single solid shell. Some research suggests that filaments grouped with a separation distance much smaller than the outer sheath edge, behave comparably to single solid-shell body[8].

This architecture offers the advantages of a spherical geometry with a significant savings in mass. The filaments form a Faraday cage that self-inflates with charge. Further, the spacecraft within the cage has superior access to solar power and telecommunications than would a spacecraft within a solid shell. Simple calculations indicate that less than 5% of the chip's surface might be shadowed by a filament structure. Like the sphere, the mesh can be compacted for launch and then passively expanded by charging.

d. Electrets

For the sake of completeness, we reference a means of volumetric charge storage that we have explored but choose not to incorporate into our design: electrets. Electrets are insulators that are artificially implanted with ions to create a quasi-permanent biased charge. The ions are mechanically bound within the material, creating an electric field.

Applications to integrated circuits have motivated research into silicon-based electrets. Thin films of insulating material are bombarded with high energy ions to yield high charge-to-mass ratios. Teflon variants, for example, suggest charge to mass ratios on the order of 10 mC/kg (Ref. 15). Concern with electrets stems from their charge lifetime. In laboratory applications, electrets typically maintain their charge integrity on the order of years. However, it remains to evaluate this timeframe in the space plasma environment. Presumably, high energy particle bombardment would reduce it beyond a useful mission life. However, these materials have yet to be evaluated fully for their application to LAO spacecraft.

Among these four architectures, a spherically shaped mesh anode and a filament cathode offer an effective architecture in terms of mass efficiency, charge density, and ease of system integration. The appropriate charging model for the "mesh" anode is the source of some uncertainty. It stands to reason that the filament separation distance dictates whether the sphere is "seen" by the plasma as a single entity experiencing sheath-related ram charging, or as a set of filaments individually charging according to OML theory. With this in mind, we selected the Debye length as the separation distance, evaluated both methods, and count on the more conservative of the two results.

With an architecture selected, we find that the details of the design are dictated by the plasma conditions, anode size and potential, and chip mass. Figure 9 shows the solution flow-diagram for a system analysis using ram-charging as the defining current. Likewise, Figure 10 gives the solution flow-diagram for the OML charging model of the mesh sphere anode. The important resulting design parameters are given in bold outline. In this flow, the anode architecture is used to determine the value of the dominant ion current. A simple current balance demonstrates that this current, though driven by the solar cell array, is supplied by the cathode. The length of the filament is then found by setting the ion current equal to the cathode filament's OML current. This enables the differential charging and leads to the final charge-to-mass ratio.

Both ram and OML charging were incorporated into models and used to evaluate a large series of anode radii and potentials for a 1 cm square silicon chip in plasma at 350 km. The result of these calculations is a map of the available charge-to-mass ratio over the anode's design space. Figure 11 presents these results as contours of charge-to-mass in C/kg are given over a logarithmic range of sphere radii and potentials.

An important output of the solution flow-diagram is the required solar cell array area, dictated by the required power and the solar cell array's efficiency. The shaded regions in Figure 11 correspond to anode designs that require more surface area than is available on one side of the silicon chip. This requirement restricts the available design space to a combination of small radii and low potentials.

Reviewing the unshaded regions in Figure 11, charge-to-mass ratios as high as 7 μC/kg can be achieved. After considering charge-to-mass ratio, available surface area for spacecraft subsystems, and simplicity of use; we select a radius corresponding to the corner-distance of the chip ($\sqrt{2}$ cm) and a potential of 200 V. These choices enable the chip to be placed within the sphere and attached at the corners, ensuring a constant orientation. With these parameters, the OML current model yields a charge-to-mass ratio of 2.92 μC/kg and the ram current model yields 2.55 μC/kg. For the sake of conservatism, we adopt 2.5 μC/kg in further estimates.

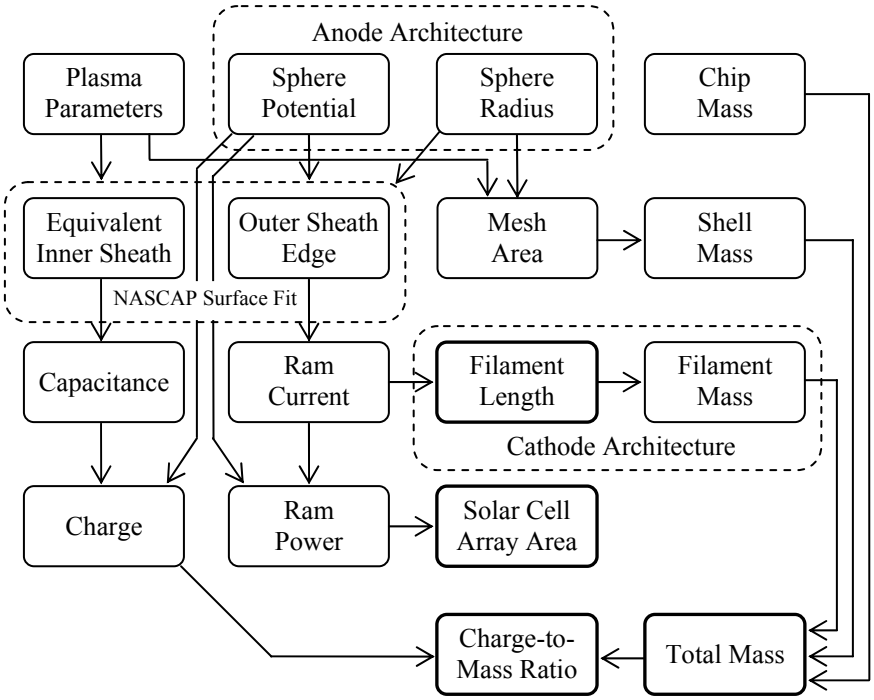

Figure 9. Solution Flow-Diagram for a differentially charged architecture with sheath currents associated with ram charging.

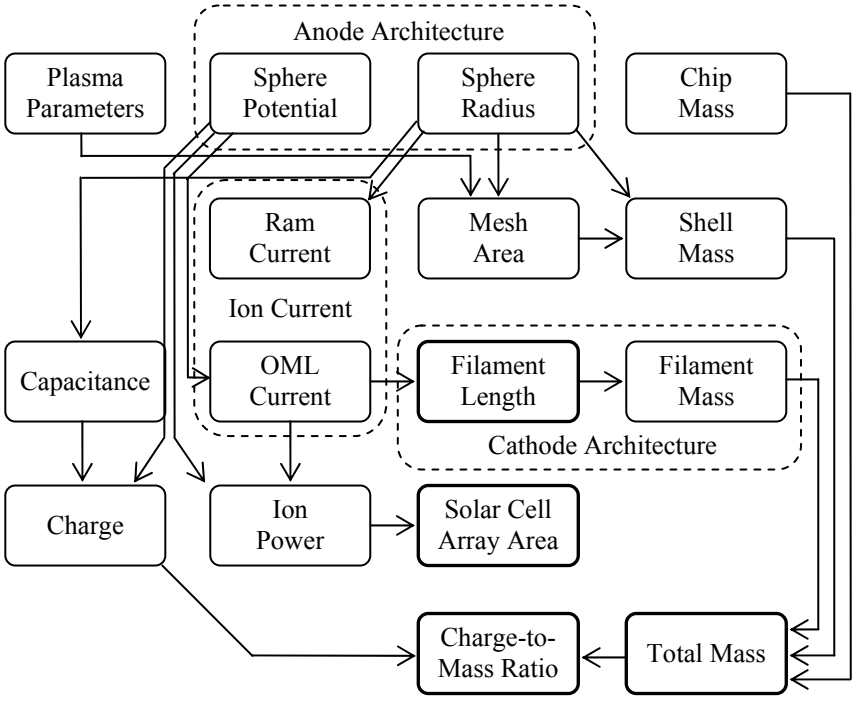

Figure 10. Solution Flow-Diagram for a differentially charged architecture with sheath currents associated with OML charging.

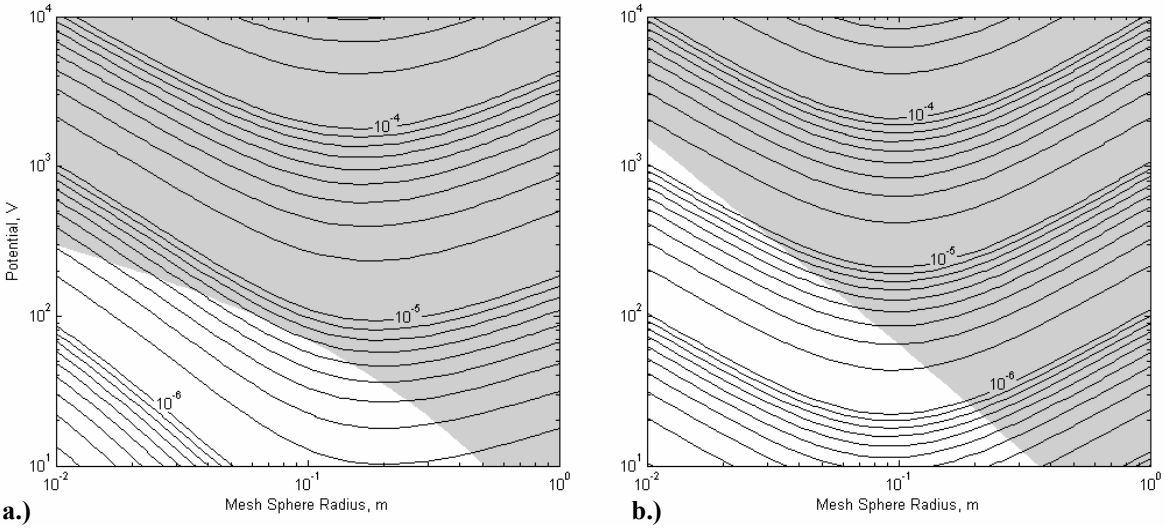

Figure 11. Contours of charge-to-mass in C/kg for mesh sphere anode over ranges of radii and potential for a.) a ram charging dominated model and b.) an OML charging model. The shaded region indicates solutions requiring more solar-cell area than is available on one side of the chip.

3. Telecommunications

Inspired by Sputnik, the communication system is intended to be a periodic beacon. The frequency of each pulse communicates the spacecraft's temperature. This section reviews relevant topics. Research in each is currently being pursued.

To ensure that the signal can be tracked from a ground station, it must be powerful enough to overcome atmospheric attenuation and other noise sources. The communication link's carrier-to-noise-ratio *C/N* is a useful measure of goodness. This ratio is influenced by the signal's frequency, the orbit's altitude, the transmitter's losses and power, atmospheric conditions, and antenna efficiency. We can accomplish only so much on this chip. A simple way to improve the downlink is to select a high-gain ground station. We propose to use one of the Deep Space Exploration Society's two 60 foot diameter parabolic dishes located in a radio-quiet region of Colorado. With an antenna gain of 43 dB, this dish represents an extremely powerful publicly accessible receiver.

A beacon pulse signal is well suited for our mission. A simple RC charging circuit can produce periodic bursts of power via transistor switching as illustrated in Figure 12. Solar power charges the capacitor until the transistor is opened, releasing the stored energy. This energy is sent through an oscillator and is emitted as RF energy via two antennas. This sequence results in a pulsed oscillating signal as depicted in Figure 13.

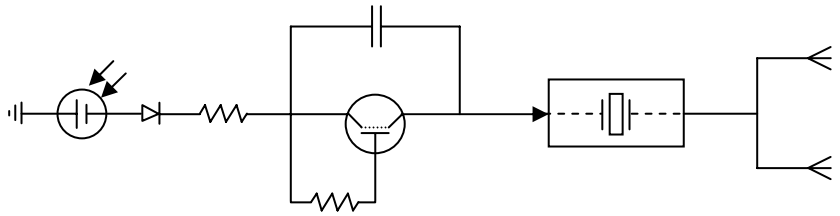

Figure 12. Conceptual circuit diagram to generate periodic RF pulses from solar flux.

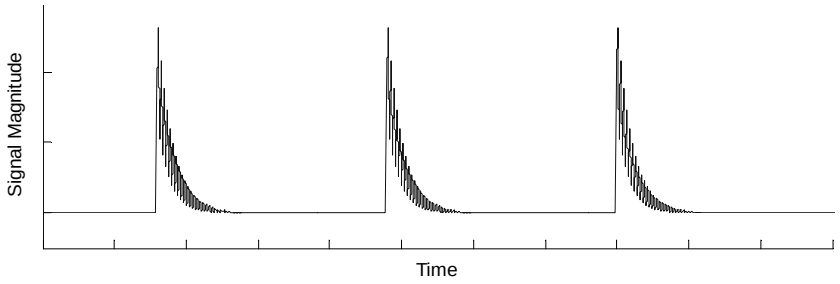

Thin-film deposition allows the fabrication of multi-layered parallel plate capacitors directly alongside other integrated circuit components. By alternatively depositing layers of metal and dielectric, charge can be stored efficiently over a given surface area. We use area-capacitance density as a metric in allocating the surface area of our wafer. Typical thin film capacitors, such as Metal-Insulator-Metal (MIM) achieve area-capacitance densities on the order of 10 nF/cm^2. This performance can be improved by treating the surfaces between the plates and incorporating high-dielectric materials, notably ceramics.

For the oscillator illustrated in Figure 12, the trade space has included an analog RLC circuit and a crystal oscillator. Though RLC circuit production is trivial at macroscopic scales, inductors are not well suited for microfabrication techniques. Research suggests that inductors on the order of 0.1 H/mm^2 can be reliably produced, though the process in challenging. A second order RLC system resonates with a natural frequency of

$$\omega_{RLC} = \frac{1}{\sqrt{L_{tc} C_{rc}}} \tag{31}$$

where C is capacitance in Farads and L is inductance in Henries. At the millimeter scale, this range of capacitance (1 μF/mm^2) and inductance (0.1 μH/mm^2) yields a natural frequency on the order of 100 kHz. Alternatively, an RLC circuit can be reproduced using a crystal piezoelectric oscillator. When subjected to an electric field, a piezoelectric crystal deforms. As the field is removed, it mechanically returns to its natural state, a process that in turn creates an opposing electric field. This process repeats, resulting in an oscillating electric signal that can be modeled as the RLC circuit in Figure 14.

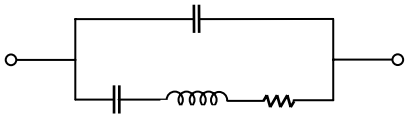

Figure 14. Piezoelectric crystal equivalent-analog circuit.

The carrier frequency of the oscillator is another key parameter. Beyond dictating the necessary signal power and oscillator design, the frequency must conform to international law. The Federal Communications Commission (FCC) restricts transmissions to specific frequency ranges and power levels[16]. The influence of the frequency choice on signal attenuation is shown in Figure 15. It is difficult to imagine that our SOC spacecraft will have sufficient power to exceed the FCC limits at any frequency.

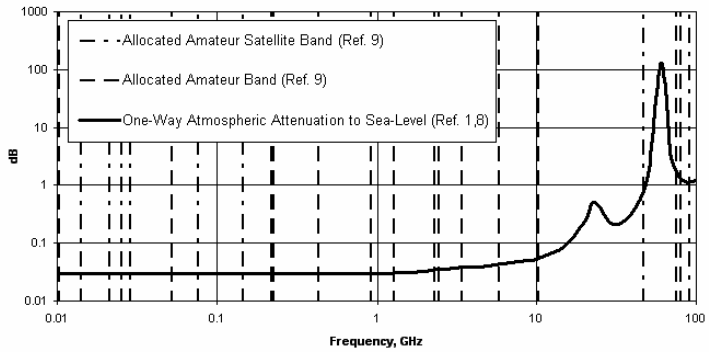

Figure 15. FCC allocated amateur bands superimposed over a model for one-way atmospheric attenuation to sea-level (7.5 g/m^3 water vapor).

Finally, it remains to discuss the antenna, a well researched topic in the microfabrication industry. Since attitude control is limited, directionality cannot be a design driver. If printed directly on the chip, only half of the energy will be radiated outward. Alternatively, one or more antennas could be mechanically attached to the circuit in the post-production and packaging fabrication steps. Though this approach would increase the antenna efficiency and enable a greater range of frequencies, it conflicts with our mass- and cost-saving goals that inspire a completely integrated spacecraft.

Two antenna styles seem most practical, having been fabricated and demonstrated at our size scales: a linear dipole antenna and a loop dipole antenna. Dipole antennas can be designed for a resonant frequency by sizing the length at full, half, or quarter wavelengths. Using a quarter-wave dipole, a centimeter length limit constrains the minimum antenna resonant frequency to approximately 7.5 GHz. The second option, a loop antenna, offers increased gain over a dipole but also has equally restrictive frequency limits. For example, a 1 cm x 1 cm square loop yields a minimum resonance of approximately 8 GHz. Based on frequency allocation, ground-station capabilities, and atmospheric attenuation; these minimum frequencies may dictate limit the transmitter's design.

4. Attitude Determination and Control

Our proposed method of LAO via differentially charged bodies offers a passive method of attitude control. Figure 16 illustrates a sphere anode and filament cathode with center of mass moving at angular velocity ω_+. The two oppositely charged geometries experience Lorentz forces in opposite radial directions concentrated at their respective centers of charge. If the spacecraft is perturbed from a radial alignment by angle α, these forces apply a restoring torque. Thus the system behaves as a simple harmonic oscillator with an equilibrium at $\alpha = 0$. This finding implies that the charged spacecraft's attitude is passively controlled by the same mechanism altering its orbit. Thus our spacecraft achieves a stable orbit-radial attitude with no additional mass, power, or system complexity. Because the orbit is circular, the spacecraft's attitude is constant with respect to nadir, offering the further advantage of ensuring the inside face of the chip always points towards Earth. This alignment ensures consistent antenna coverage for telecommunications.

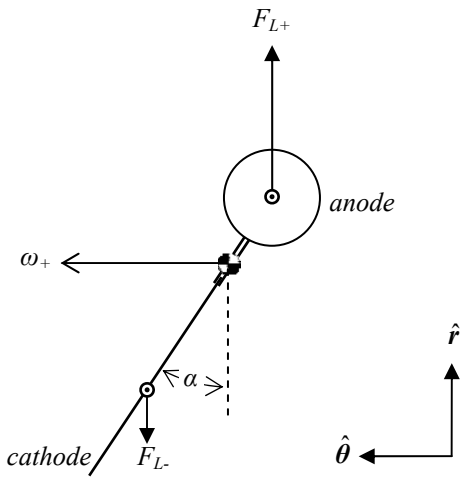

Figure 16. Illustration of differentially charged bodies subject to opposite Lorentz forces and free to rotate about the center of mass

For completeness we include discussion of another architecture we considered but chose not to pursue in this application: outgassing. Outgassing is the spontaneous evolution of a gas from a solid or liquid in the presence of a low-pressure environment. Spacecraft are built of low-outgassing materials in order to prevent the evolving gas cloud from corrupting sensors and payloads, from torquing the spacecraft, and from causing materials-related failures. As particles outgas from the surface, momentum is imparted to the spacecraft. By selectively applying an outgassing agent to the corners of the wafer, this momentum can be used to generate a torque on the spacecraft. This mechanism was observed as on the Microwave Anisotropy Probe spacecraft. There it caused undesirable change in angular momentum[17]. Once spinning, a SOC can use magnetic torque coils to precess the spinning attitude for active pointing. Such actuators scale well to the SOC and can be integrated easily as loop-shaped traces.

5. Structure

The structure of the spacecraft consists of the single silicon chip. Though a gallium arsenide substrate offers improved radiation resistance and photovoltaic properties, it is not as readily used in standard fabrication processes or tools as silicon. In order to maximize use of the available surface area, we propose double-sided printing. Alternatively, a flip-chip style of production may be employed. In this process, two chips are manufactured such that their backsides can be mated and both chips face outward. This technique allows us to incorporate devices whose fabrication techniques aren't compatible by producing them separately and integrating them at the end of production. Of primary interest is the incorporation of solar cells on both sides of the chip to ensure that power is always available, regardless of attitude.

6. Thermal Control

In orbit, the SOC's low thermal mass will result in temperatures that range between -130°C to 100°C. This variation can occur within tens of seconds[18]. Thermal stresses associated with eclipses may fatigue the chip where dissimilar metals contact. These risks, along with possible remediative strategies such as microfabricated radiator fins, have yet to be evaluated. An active means of remediation might be achieved for the spinning SOC: tilting the attitude so that the face points toward or away from the sun or the earth to might be used to control temperature.

III. Results

A.Sample Design

Our design features a 1 cm square, 500 μm thick silicon chip surrounded by an aluminum mesh sphere and attached to an 8 m aluminum filament, as illustrated in Figure 17. Solar cells printed directly onto the chip supply 200 V at 48 μA to the sphere and filament when oriented as much as 45° from the sun. The sphere attains a negative potential (-190 V), and the filament's potential is weakly positive (+10 V). The two are separated by an insulated conductor that is longer than their combined outer sheath sizes to prevent plasma interactions. The system-level charge-to-mass ratio is -2.5 μC/kg (calculated with the more conservative OML solution), sufficient for LAO demonstration when released into a circular orbit at 350 km. The system passively orients itself along the Lorentz force's line-of-action. The total system mass amounts to less than 0.15 g.

A separate solar array charges a capacitor designed to report the spacecraft's temperature as an RF pulse through a small antenna. Each side of the spacecraft is identical, to reduce solar array shadowing and transmission loss. Tables 6, 7, and 8 give further design budgets and parameters.

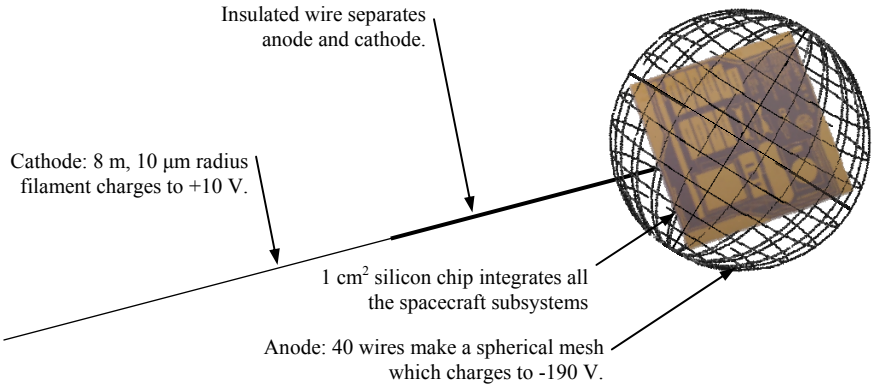

Figure 17. An illustration of our sample spacecraft architecture.

Table 4. Minimum Mass Budget

Subsystem	Mass, mg
Propulsion (Anode / Cathode)	8
Telecommunications	0, (Printed onto structure)
Power	0, (Printed onto structure)
Attitude Determination and Control	0, Passive
Structure	115
Total	123

Table 5. Surface Area Budget

Subsystem	Surface Area per Side, mm^2
Power	98
Telecommunications	Remainder
Attitude Determination and Control	0, Passive
Total	157

Table 6. Selected Power and Propulsion Parameters

Parameter	Selection / Result
Orbit	Circular
Altitude, km	350
Quasi-Neutral Number Density, m^{-3}	1E12
Quasi-Neutral Temperature, eV	0.1
Charging Method	Differential Charging
Potential Difference, V	200
Charge Storage	Mesh Sphere / Filament
Material	Aluminum
Filament Radius, m	1E-5
Length Density, kg/m^2	8.48E-7
Mesh Sphere Anode	
Radius, cm	$\sqrt{2}$
Number of Filaments in Mesh	40
Filament Separation at diameter	1 Debye length
Total Length of Mesh, m	1.8
Total Mass, mg	1.5
Outer Sheath Edge, m	0.14
Equivalent Radius Sheath Size, m	0.070
Filament Cathode	
Length of Filament, m	8.0
Mass, mg	6.8
Outer Sheath Edge, m	< 0.1
Insulated Conductor Length, m	0.25
Solar Cell Array	
Specific Power	100 W/kg
Efficiency	10%
Estimated Floating Potential, V	-190 / +10
Net Charge, C	3.59E-10
Ram Current, μA	48.5
Estimated Charge to Mass Ratio, μC/kg	2.5
Maximum Along-Track Separation, m/day	17.8

IV. Conclusion

We have motivated research into micro-scale design and fabrication of spacecraft components based on orbital dynamics, plasma effects, and propellantless technology. The result of these efforts is a candidate architecture for a fully integrated "Spacecraft on a Chip" capable of passively altering its orbit via the Lorentz force. Based on this work, we conclude that the concept is indeed viable, and the project is worth pursuing both for the sake of spacecraft integration and Lorentz Orbit Augmentation. Our current and future work focuses on addressing the telecommunications subsystem design, devising a robust procedure for estimating the spacecraft's orbit, and developing microfabrication process-diagrams. Ultimately, we intend to produce and launch the first Lorentz-propelled millimeter-scale spacecraft.

References

[1] Peck, M. A., Prospects and Challenges of Lorentz Augmented Orbits," Submitted for Publication. AIAA Journal of Spacecraft and Rockets. 2006.

[2] Streetman, B. and Peck, M., "Synchronous Orbits and Disturbance Rejection Using the Geomagnetic Lorentz Force" Proceedings of the AIAA Guidance, Navigation, and Control Conference, August 2006.

[3] Hillard G. B. and Ferguson, D. C., "Low Earth Orbit Spacecraft Charging Design Guidelines," NASA/TP-2003-212287, February 2003.

[4] Whipple. E. C., "Potentials of Surfaces in Space," Reports on Progress in Physics, Vol. 44, 1981, pp. 1217

[5] Blackwell D. D., Walker, D. N., Messer, S. J., and Amatucci, W.E., "Characteristics of the Plasma Impedance Probe with Constant Bias," Physics of Plasmas, Vol 12. 2005.

[6] Laframboise, J. G., Ph.D. thesis, University of Toronto, Institute for Aerospace Studies, Report No. 100, 1966.

[7] Parker, L.W., "Plasmasheath-Photosheath Theory for Large High-Voltage Space Structures," AIAA, 1980. p. 507-509.

[8] Choinière, E., "Theory and Experimental Evaluation of a Consistent Steady-State Kinetic Model for 2-D Conductive Structures in Ionospheric Plasmas with Applications to Bare Electrodynamic Tethers in Space," Ph.D. thesis, University of Michigan, 2004.

[9] Hoyt, R. P., and Minor, B. M., "Remediation of Radiation Belts Using Electrostatic Tether Structures," Tethers Unlimited Inc., 2004.

[10] Kasha, M.A., "The Ionosphere and Its Interaction with Satellites," Gordon and Breach, New York, 1969.

[11] Geuther, J.A. and Danon, Y., "Electron and Positive Ion Acceleration with Pyroelectric Crystals," Journal of Applied Physics, Vol. 97, 2005.

[12] Rossi, C., Larangot, B., Pham, P.Q., Briand, D., de Roij, N.F., Puig-Vidal, M., and Samitier, J., "Solid Propellant Microthrusters on Silicon: Design, Modeling, Fabrication, and Testing," Journal of Microelectromechanical Systems, Vol. 15, No. 6, 2006.

[13] Talley, C., Clayton, W., Gierow, J., McGee., J and Moore, J., "Advanced Membrane Materials for Improved Solar Sail Capabilities," 43rd AIAA/ASME/ASCE/AHS/ASC Structures, Structural Dynamics, and Materials Conference: 3rd AIAA Gossamer Spacecraft Forum, 2002.

[14] Cosmo, M. and Lorenzini, E. Editors, "Tethers in Space Handbook," 3rd ed, 1997.

[15] Kressmann, R., Sessler, G. M., and Günther, P., "Space-charge Electets," IEEE Transactions on Dielectrics and Electrical Insulation, Vol. 3, No. 5, 1996.

[16] U.S. Department of Commerce, National Telecommunications and Information Administration, Office of Spectrum Management, "United States Frequency Allocations – The Radio Spectrum," October 2003.

[17] Starin, S. R. et al, "An Anomalous Force on the MAP Spacecraft," 2002 AIAA Symposium, Monterey, CA.

[18] Gilmore, D. G., Hardt, B. E., Prager, R. C., Grob E. W. and Ousley, W., "Thermal Systems," Spacecraft Mission Analysis and Design, 3rd ed., Microcosm Press and Kluwer Academic Publishers. 2005.